Original articles

A spectral collocation scheme for the two dimensional flow of a regularized viscoplastic fluid: Numerical results and comparison with analytical solution

Lorenzo Fusi [*], Antonio Giovinetto

Università degli Studi di Firenze, Dipartimento di Matematica e Informatica "Ulisse Dini", Viale Morgagni 67/A, 50134 Firenze, Italy

ARTICLE INFO

ABSTRACT

In this paper we present a numerical scheme based on spectral collocation method (SCM) for the two dimensional incompressible creeping flow of a non-Newtonian fluid in a symmetric channel of variable width. Afters a suitable scaling of the governing equations and of the boundary conditions, we discretize the problem getting a nonlinear system that is solved via Newton–Raphson method. We focus on two regularized viscoplastic fluids (Bingham, Casson), but the method can be applied to any fluid in which the apparent viscosity depends on the modulus of the strain rate tensor. In the case of small aspect ratio of the channel we explicitly determine the lubrication solution at the leading order and we prove some symmetry properties. We validate the numerical scheme through a comparison with the analytical solution, showing an excellent agreement between the latter and the numerical solution. We consider three types of wall functions (convergent, divergent and non-monotone) and we perform numerical simulations for channels with general aspect ratio. We observe that the symmetries of the lubrication solution are maintained also when the characteristic length and width of the channel are of the same order. We have proved that the monotonicity of the yield surface follows the one of the channel profile when the aspect ratio of the channel is "sufficiently small". This is no longer true when the latter hypothesis is removed.

1. Introduction

Viscoplastic fluids are characterized by a yield stress that must be overcome to start the flow, see [21]. The constitutive equation of a viscoplastic material allows one to divide the domain in yielded and unyielded regions. In the unyielded region the modulus of the deviatoric stress is below the critical threshold, so that no deformation is possible and the fluid behaves as a rigid body. The surface that divides the yielded and the unyielded domain, called yield surface, is a priori unknown and must be determined imposing appropriate boundary conditions (free boundary problem). The simplest viscoplastic fluid is the so-called Bingham fluid [3], which is characterized by a linear stress/strain-rate relation above the critical threshold. More complex models with nonlinear stress/strain-rate relation can also be considered (Herschel–Bulkley, Casson, etc., see [5,19]).

In a viscoplastic fluid, when the rate of deformation is zero the rheological model presents a singularity due to the apparent viscosity that becomes infinite (rigid body behavior). This singularity produces significant numerical and analytical problems in the solution of the mathematical problem, in particular in the detection of the yield surface. The inspiration for this work comes from the necessity of finding appropriate approximations (regularized models) capable of smoothing such singularity. In this optics, one can

---

* Corresponding author.
  E-mail address: lorenzo.fusi@unifi.it (L. Fusi).

consider regularized models, such as the Papanastasiou or the Bercovier–Engelman models, see [1,28]. The idea of regularization is natural, from both physical and mathematical perspectives. In the regularized models the singularity is smoothed through a sufficiently regular viscosity function that approximates the exact model. Of course, one has an infinity of suitable choices for the approximating function. There is an ongoing debate on whether the regularized models are of some help or not, since it is well known that some of the properties of the exact viscoplastic fluid are not recovered when the approximated model tends to the exact one, see for instance [8,13]. Other strategies aimed at overcoming the singularity issues of the exact model are also possible. Among these, we mention the one in which the unyielded region is treated as an elastic or viscoelastic solid, [12,14].

The creeping flow of viscoplastic fluids in a two-dimensional channel of varying width has been widely studied in the past decades, see [21] and the references therein. Analytical solutions can be obtained for particular geometrical settings (e.g. lubrication flows) for both "true" viscoplastic and regularized flows, [6,9,13,15,24–27,30,35]. Many numerical methods have been employed to investigate the flow behavior of exact and regularized viscoplastic fluids in more general geometrical settings, [16,22,23], [7].

In this paper we present a spectral collocation scheme (similar to the one employed in [29]) to investigate the two-dimensional creeping flow of a "regularized viscoplastic fluid" in a symmetric channel of non-uniform width driven by an applied pressure gradient (plane Poiseuille flow). This approach, which is much simpler than other methods like finite element methods or finite volume methods, also requiring less CPU time, has not been employed for this type of problems. We limit our analysis to a regularized Bingham fluid and a regularized Casson fluid, but the scheme can also be applied to any generalized Newtonian fluid, i.e. any fluid in which the apparent viscosity depends on the modulus of the strain rate tensor (Power-law, Cross, Carreau, etc.). To the authors' knowledge spectral methods have never been employed for the channel flow of viscoplastic fluids. The main numerical approaches, i.e. regularization and augmented Lagrangian methods are typically implemented in finite elements/volume discretization, [32].

From the point of view of possible applications, this work can be useful in all the situations in which one has to solve flow problems that can be approximated by a non uniform 2D geometry, e.g. flow of muds, slurries, waxy oils or any industrial viscoplastic fluids in closed channels. The importance of this study is not tied therefore to any particular application.

The mathematical problem consists of mass and momentum balance to which we add no-slip wall conditions plus inlet/outlet pressure conditions. In a 2D non uniform channel this problem is well posed, see [2]. The problem is reformulated in a dimensionless form and the flow domain is mapped in the square $[-1, 1]^2$ so that the discretized spectral differentiation operators can be applied. The problem is written in the first order velocity–stress–pressure formulation in which the stress components are treated as unknowns. The discretized problem consists of a nonlinear system plus boundary conditions. The adding of the boundary conditions to the discretized problem leads to a nonlinear overdetermined system that is solved via least-squares and exploiting Newton's method, see [17,18]. The advantage of using least-squares is that this method results in a symmetric and positive definite algebraic system which circumvents the well known LBB (Ladyzhenskaya–Babuška–Brezzi) condition, see [4].

To validate the numerical model we make a comparison between the numerical solution and the analytical solution that one can explicitly find if the aspect ratio of the channel is sufficiently small (lubrication approximation). Indeed, in the case of small aspect ratio, the solution can be sought in the form of an asymptotic expansion around the small ratio parameter, in which each term of the expansion can be determined by an iterative process. In particular, we shall compare the "leading order" solution with the general numerical solution obtained through the least-square spectral collocation method. We will see that the agreement between the two is excellent. We shall also prove some properties of symmetry of the analytical solution (small aspect ratio solution) that remain valid also for the general numerical solution (any aspect ratio).

The main novelty is the adoption of a numerical scheme based on spectral collocation methods, which are more flexible and of easy implementation than other methods (e.g. finite differences, finite elements and finite volumes). We have focused on regularized viscoplastic fluids because the approximated models allow one to overcome the singularities issues inherently present in this type of fluids. It should also be noticed that this method is highly versatile, since a simple change of the viscosity function allows one to deal not only with any type of generalized Newtonian fluid, but also with fluids of implicit type, such as fluids with pressure dependent viscosity [20]. The principal research question this paper sets out to answer to is the detection of the yield surface and the dependence of the latter on 1) the rheological parameters; 2) on the geometry of the system; 3) on the applied pressure drop.

2. The mathematical model

Let us consider an incompressible generalized Newtonian fluid where the apparent viscosity depends on the strain-rate modulus,[1] i.e. $\mu^* := \mu^*(\dot\gamma^*)$, where

$$\dot\gamma^* := \sqrt{\frac{1}{2}\mathrm{tr}\left(\mathbb{D}^{*2}\right)}, \tag{1}$$

is the Frobenius norm of the symmetric part of the velocity gradient $\mathbb{D}$. The Cauchy stress tensor is written as

$$\mathbb{T}^* = -p^*\mathbb{I} + 2\mu^*(\dot\gamma^*)\mathbb{D}^*, \tag{2}$$

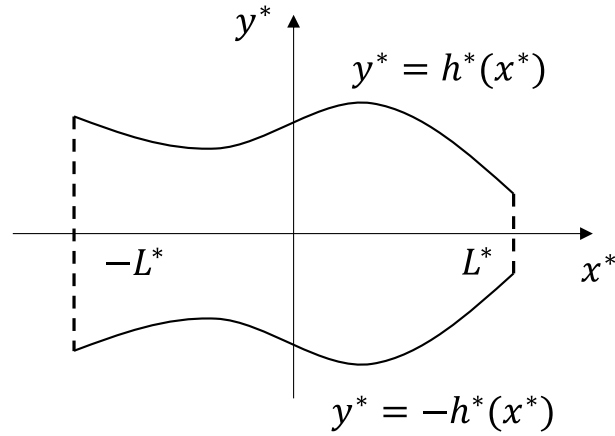[1] In the paper the starred quantities denote dimensional variables.

Fig. 1. Sketch of the domain of the problem. A two-dimensional channel with non-flat walls. The channel profile is assumed to be C^1.

where $\mathbb{S}^* =: 2\mu^*(\dot{\gamma}^*)\mathbb{D}^*$ is the deviatoric part of the stress and $-p^*\mathbb{I}$ is the spherical part, p^* being the Lagrange multiplier due to the incompressibility constraint (pressure). Mass and momentum balance, in the absence of body forces, yield (see [34])

$$\begin{cases} \rho^* \dfrac{D\mathbf{v}^*}{Dt^*} = -\nabla^* p^* + \nabla^* \cdot \mathbb{S}^*, \\[2mm] \nabla^* \cdot \mathbf{v}^* = 0, \end{cases} \tag{3}$$

ρ^* being the constant density of the fluid and $\mathbf{v}^*$ the velocity field. We consider a 2D flow in a channel of length L^* bounded by the rigid walls $y^* = \pm h^*(x^*)$, $h^*(x^*)$ being a sufficiently regular positive function defined in $[-L^*, L^*]$, see Fig. 1. The function $h^*(x^*)$ that defines the channel profile can be of any type, provided it is sufficiently regular (C^1). Because of this general geometrical setting, our study can be applied to all applications in which the flow can be considered two dimensional and symmetric.

The flow is driven by the pressure drop $\Delta p^* = p_{in}^* - p_{out}^*$, where p_{in}^* and p_{out}^* are the pressure at the inlet and outlet respectively. The velocity $\mathbf{v}^*$ is given by

$$\mathbf{v}^*(x^*, y^*, t^*) = u^*(x^*, y^*, t^*)\mathbf{e}_1 + v^*(x^*, y^*, t^*)\mathbf{e}_2. \tag{4}$$

The boundary conditions for the velocity field are no-slip at the channel walls and null transversal velocity at the inlet and outlet:

$$\mathbf{v}^*(x^*, h^*(x^*), t^*) = 0, \qquad \mathbf{v}^*(\pm L^*, y^*, t^*) \cdot (0, 1) = 0. \tag{5}$$

The boundary conditions for the pressure are given imposing the inlet and outlet pressure:

$$p^*(-L^*, y^*, t^*) = p_{in}^*, \qquad p^*(L^*, y^*, t^*) = p_{out}^*. \tag{6}$$

With these boundary conditions, problem (3) is well posed, see [2]. We shall limit our study to the following types of apparent viscosities

$$\mu^*(\dot{\gamma}^*) = \left(\mu_o^* + \frac{\tau_y^*}{\dot{\gamma}^* + \varepsilon^*} \right), \qquad \text{(Regularized Bingham)} \tag{7}$$

$$\mu^*(\dot{\gamma}^*) = \left(\sqrt{\mu_o^*} + \frac{\sqrt{\tau_y^*}}{\sqrt{\dot{\gamma}^*} + \sqrt{\varepsilon^*}} \right)^2, \qquad \text{(Regularized Casson)} \tag{8}$$

where μ_o^* is a characteristic viscosity, τ_y^* is the yield stress and ε^* is a regularization parameter with the dimension of a strain rate. The constitutive laws (7), (8) are those of a regularized Bingham fluid and of a regularized Casson fluid. From (7), (8) we notice that for $\varepsilon^* \to 0$ we recover the exact Bingham and Casson models, while for $\varepsilon^* \to \infty$ we recover the classical Navier–Stokes incompressible model.

3. Non-dimensional formulation

We define

$$H^* = \sup_{x^* \in [-L^*, \, L^*]} h^*(x^*), \qquad \delta = \frac{H^*}{L^*}, \tag{9}$$

and we rescale the variables as follows

$$
\begin{cases}
x = \dfrac{x^*}{L^*}, \quad y = \dfrac{y^*}{H^*}, \quad t = \left(\dfrac{U^*}{L^*}\right)t^*, \quad u = \dfrac{u^*}{U^*}, \quad v = \dfrac{v^*}{\delta U^*}; \quad p = \dfrac{p^* - p_{out}^*}{P^*}, \\[3mm]
\mathbb{D} = \left(\dfrac{H^*}{U^*}\right)\mathbb{D}^*, \quad \mathbb{S} = \left(\dfrac{H^*}{\mu_o^* U^*}\right)\mathbb{S}^*, \quad \dot{\gamma} = \left(\dfrac{H^*}{U^*}\right)\dot{\gamma}^*, \quad \mu = \dfrac{\mu^*(\dot{\gamma})}{\mu_o^*},
\end{cases}
\tag{10}
$$

where U^* and P^* are the characteristic velocity and pressure respectively. We get

$$
\mathbb{D} = \frac{1}{2}\begin{bmatrix} 2\delta u_x & u_y + \delta^2 v_x \\ u_y + \delta^2 v_x & 2\delta v_y \end{bmatrix}, \quad \mathbb{S} = 2\mu(\dot{\gamma})\,\mathbb{D} = \begin{bmatrix} S_{11} & S_{12} \\ S_{21} & S_{22} \end{bmatrix},
$$

$$
\dot{\gamma} = \sqrt{\delta^2\left(u_x\right)^2 + \frac{1}{4}\left(u_y + \delta^2 v_x\right)^2}.
\tag{11}
$$

The non dimensional versions of (7), (8) are

$$
\mu(\dot{\gamma}) = \left(1 + \frac{B}{\dot{\gamma} + \varepsilon}\right), \qquad \text{(Regularized Bingham)}
\tag{12}
$$

$$
\mu(\dot{\gamma}) = \left(1 + \frac{\sqrt{B}}{\sqrt{\dot{\gamma}} + \sqrt{\varepsilon}}\right)^2, \qquad \text{(Regularized Casson)}
\tag{13}
$$

where

$$
B = \left(\frac{\tau_y^* H^*}{\mu_o U^*}\right), \qquad \varepsilon = \left(\frac{H^*}{U^*}\right)\varepsilon^*,
\tag{14}
$$

B being the Bingham number. Selecting $P^* = (\mu_o^* U^* L^*)/H^{*2}$, we can write the momentum balance component-wise

$$
\begin{cases}
Re\delta\left(u_t + u_x u + u_y v\right) = -p_x + \delta(S_{11})_x + (S_{12})_y, \\[2mm]
Re\delta^3\left(v_t + v_x u + v_y v\right) = -p_y + \delta^2(S_{12})_x + \delta(S_{22})_y,
\end{cases}
\tag{15}
$$

where $Re := (\rho^* U^* H^*)/\mu_o^*$ is the Reynolds number. Finally, assuming $Re \ll 1$ (creeping flow) and rescaling $h^*(x^*)$ with H^* we write the complete system in the stress-based formulation

$$
\begin{cases}
-p_x + \delta(S_{11})_x + (S_{12})_y = 0, \\[2mm]
-p_y + \delta^2(S_{12})_x + \delta(S_{22})_y = 0, \\[2mm]
S_{11} = 2\delta\mu(\dot{\gamma})\,u_x, \\[2mm]
S_{12} = \mu(\dot{\gamma})\left(u_y + \delta^2 v_x\right), \\[2mm]
S_{22} = 2\delta\mu(\dot{\gamma})\,v_y, \\[2mm]
u_x + v_y = 0, \\[2mm]
u|_{y=\pm h(x)} = v|_{y=\pm h(x)} = 0, \\[2mm]
p|_{x=-1} = p_{in}, \qquad p|_{x=1} = 0, \qquad v|_{x=\pm 1} = 0,
\end{cases}
\tag{16}
$$

where

$$
p_{in} = \frac{p_{in}^* - p_{out}^*}{\left(\dfrac{\mu_o U^*}{\delta H^*}\right)} > 0.
\tag{17}
$$

The system (16) is well posed (see [2]) in the unknowns S_{11}, S_{12}, S_{22}, u, v, p and will be solved numerically in the next section.

Remark 1. In the Bingham (or Casson) model the unyielded regions are those for which $|\mathbb{S}| \leqslant B$ or equivalently those for which $\mathbb{D} \equiv 0$. In the regularized models the unyielded regions are approximated by those for which $|\mathbb{S}| \leqslant B$ even if $\mathbb{D} \not\equiv 0$ in such regions. Indeed, the regularized models are "seemingly" viscoplastic (they do not have a real yield stress) and not "truly viscoplastic".

Let us now focus on the third condition of $(16)_8$. We observe that $v(\pm 1, y) = 0$, so that

$$
v_y(\pm 1, y) \underbrace{=}_{\text{mass balance}} -u_x(\pm 1, y) = 0.
\tag{18}
$$

Moreover, because of symmetry with respect to the central plane $y = 0$, we also have

$$
u_y(x, 0) = v(x, 0) = v_x(x, 0) = 0.
\tag{19}
$$

Hence, recalling the definition (11) we get

$$\dot{\gamma}(\pm 1, 0) = 0, \tag{20}$$

so that $(\pm 1, 0)$ are points with zero shear rate. This means that there exist neighborhoods of $(\pm 1, 0)$ in which the fluid is unyielded in the sense explained above ($|\mathbb{S}| \leqslant B$). When $B = 0$ these regions reduce to the points $(\pm 1, 0)$.

4. Numerical scheme

The basic domain for the application of the Spectral Collocation Method is the square centered at the origin of the Cartesian system with side length two, i.e. $[-1, 1]^2$. In order to map the flow domain in the computational domain $[-1, 1]^2$ we consider the following transformation of coordinates:

$$\xi = x, \qquad \eta = \frac{y}{h(x)} \in [-1, \ 1]. \tag{21}$$

We write system (16) for the new coordinates (ξ, η), introducing the new variables:

$$u(x, y) = \widehat{u}(\xi, \eta), \qquad v(x, y) = \widehat{v}(\xi, \eta), \qquad p(x, y) = \widehat{p}(\xi, \eta), \tag{22}$$

$$S_{11}(x, y) = \widehat{S}_{11}(\xi, \eta), \qquad S_{12}(x, y) = \widehat{S}_{12}(\xi, \eta), \qquad S_{22}(x, y) = \widehat{S}_{22}(\xi, \eta). \tag{23}$$

We also introduce the linear operators

$$P_1 := \partial_\xi + \left(\frac{\eta}{h(\xi)} h_\xi(\xi) \right) \partial_\eta, \qquad P_2 := \frac{1}{h(\xi)} \partial_\eta, \tag{24}$$

both defined on the function space

$$\mathcal{L}_d = \left\{ f \ : \ [-1, \ 1]^2 \to \ \mathbb{R} \ : \ f \in C^1 \left([-1, \ 1]^2 \right) \right\}. \tag{25}$$

For a generic scalar function $g(x, y) = \widehat{g}(\xi, \eta)$ we obtain that

$$g_x = P_1 \widehat{g}, \qquad \text{and} \qquad g_y = P_2 \widehat{g}. \tag{26}$$

Thus, we can write the whole problem in the new coordinate system (ξ, η) using operators P_1 and P_2. We first get the strain rate tensor, its norm and the stress tensor:

$$\widehat{\mathbb{D}}(\xi, \eta) = \frac{1}{2} \begin{bmatrix} 2\delta P_1 \widehat{u} & P_2 \widehat{u} + \delta^2 P_1 \widehat{v} \\ P_2 \widehat{u} + \delta^2 P_1 \widehat{v} & 2\delta P_2 \widehat{v} \end{bmatrix}, \tag{27}$$

$$\widehat{\gamma}(\xi, \eta) = \sqrt{\delta^2 \left(P_1 \widehat{u} \right)^2 + \frac{1}{4} \left(P_2 \widehat{u} + \delta^2 P_1 \widehat{v} \right)^2}, \tag{28}$$

$$\widehat{\mathbb{S}}(\xi, \eta) = \widehat{\mu}(\widehat{\gamma}) \begin{bmatrix} 2\delta P_1 \widehat{u} & P_2 \widehat{u} + \delta^2 P_1 \widehat{v} \\ P_2 \widehat{u} + \delta^2 P_1 \widehat{v} & 2\delta P_2 \widehat{v} \end{bmatrix}, \tag{29}$$

and then we rewrite the system (16) as follows:

$$\begin{bmatrix} \delta P_1 & P_2 & 0 & 0 & 0 & -P_1 \\ 0 & \delta^2 P_1 & \delta P_2 & 0 & 0 & -P_2 \\ 1 & 0 & 0 & -2\widehat{\mu}\delta P_1 & 0 & 0 \\ 0 & 1 & 0 & -\widehat{\mu}P_2 & -\widehat{\mu}\delta^2 P_1 & 0 \\ 0 & 0 & 1 & 0 & -2\widehat{\mu}\delta P_2 & 0 \\ 0 & 0 & 0 & P_1 & P_2 & 0 \end{bmatrix} \begin{bmatrix} \widehat{S}_{11} \\ \widehat{S}_{12} \\ \widehat{S}_{22} \\ \widehat{u} \\ \widehat{v} \\ \widehat{p} \end{bmatrix} = 0, \tag{30}$$

to which we must add the boundary conditions

$$\begin{cases} \widehat{u}|_{\eta=\pm 1} = \widehat{v}|_{\eta=\pm 1} = 0, \\ \widehat{p}|_{\xi=-1} = p_{in}, \\ \widehat{p}|_{\xi=1} = 0, \\ \widehat{v}|_{\xi=\pm 1} = 0. \end{cases} \tag{31}$$

In order to discretize the nonlinear system (30) we introduce the standard Chebyshev Gauss–Lobatto collocation nodes given by

$$(\xi_i, \eta_j) = \left(\cos \frac{(i-1)\pi}{N}, \cos \frac{(i-1)\pi}{N} \right), \qquad i, j = 1, \dots \dots \dots, N+1. \tag{32}$$
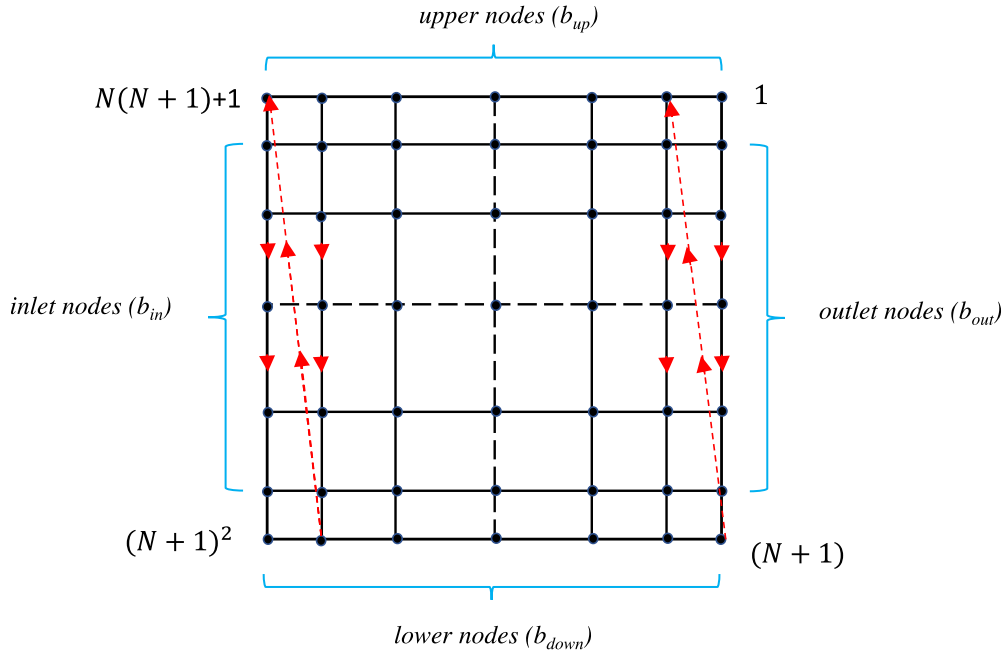
Fig. 2. Computational grid.The black circles represent the nodes of the grid.

We put the GL points in a "lexicographic" order as in [33], see Fig. 2. This means that the $(N + 1) \times (N + 1)$ array of nodes is transformed in a $(N + 1)^2$ vector ordered following the red pattern indicated in Fig. 2. We denote with b_{in} the indices[2] of the inlet nodes except corners, with b_{out} the indices of the outlet nodes except corners, with b_{up} the indices of the upper edge nodes and with b_{down} the indices of the lower edge nodes. The spectral partial derivatives in the (ξ, η) coordinate are given by

$$\partial_\xi \approx D_\xi = D \otimes_K I, \qquad \partial_\eta \approx D_\eta = I \otimes_K D, \tag{33}$$

where D is the $(N+1) \times (N+1)$ differentiation matrix defined in [33] and $\otimes_K$ is the Kronecker product. Notice that the dimensions of D_ξ, D_η are $(N+1)^2 \times (N+1)^2$. These matrices operate on functions defined on grid nodes put in the lexicographic order. Approximating the differential operators (24) using (33) and substituting into (30) we get the following nonlinear square system

$$\begin{bmatrix} \delta P_{1,N} & P_{2,N} & 0 & 0 & 0 & -P_{1,N} \\ 0 & \delta^2 P_{1,N} & \delta P_{2,N} & 0 & 0 & -P_{2,N} \\ I & 0 & 0 & -2\widehat{\mu}_N \delta P_{1,N} & 0 & 0 \\ 0 & I & 0 & -\widehat{\mu}_N P_{2,N} & -\widehat{\mu}_N \delta^2 P_{1,N} & 0 \\ 0 & 0 & I & 0 & -2\widehat{\mu}_N \delta P_{2,N} & 0 \\ 0 & 0 & 0 & P_{1,N} & P_{2,N} & 0 \end{bmatrix} \begin{bmatrix} \widehat{S}_{11,N} \\ \widehat{S}_{12,N} \\ \widehat{S}_{22,N} \\ \widehat{u}_N \\ \widehat{v}_N \\ \widehat{p}_N \end{bmatrix} = 0, \tag{34}$$

where the pedix N indicates we are considering the discretized form of the operators and variables. Notice that each of the unknowns $\widehat{S}_{11,N}$, $\widehat{S}_{12,N}$, $\widehat{S}_{22,N}$, $\widehat{u}_N$, $\widehat{v}_N$, $\widehat{p}_N$ are in the form of a vector of $(N + 1)^2$ elements, coherently with the lexicographic order of Fig. 2.

We need to add to system (34), which has dimensions $6(N + 1)^2 \times 6(N + 1)^2$, the boundary conditions. In order to do this, following [17], we define the boundary operator B_N such that

$$\underbrace{\begin{bmatrix} 0 & 0 & 0 & B_{ud,N} & 0 & 0 \\ 0 & 0 & 0 & 0 & B_{ud,N} & 0 \\ 0 & 0 & 0 & 0 & B_{io,N} & 0 \\ 0 & 0 & 0 & 0 & 0 & B_{in,N} \\ 0 & 0 & 0 & 0 & 0 & B_{out,N} \end{bmatrix}}_{= B_N} \begin{bmatrix} \widehat{S}_{11,N} \\ \widehat{S}_{12,N} \\ \widehat{S}_{22,N} \\ \widehat{u}_N \\ \widehat{v}_N \\ \widehat{p}_N \end{bmatrix} = \begin{bmatrix} 0 \\ 0 \\ 0 \\ p_{in} \\ 0 \end{bmatrix}, \tag{35}$$

where:

- $B_{ud,N}$ is the $2(N + 1) \times (N + 1)^2$ matrix whose entries are equal to one at (i, i), with $i \in b_{up} \cup b_{down}$, and zero elsewhere;

---

[2] Here the indices are considered with respect to the lexicographic order.

- $B_{io,N}$ is the $2(N-1) \times (N+1)^2$ matrix whose entries are equal to one at (i,i), with $i \in b_{in} \cup b_{out}$, and zero elsewhere;
- $B_{in,N}$ is the $(N-1) \times (N+1)^2$ matrix whose entries are equal to one at (i,i), with $i \in b_{in}$, and zero elsewhere;
- $B_{out,N}$ is the $(N-1) \times (N+1)^2$ matrix whose entries are equal to one at (i,i), with $i \in b_{out}$, and zero elsewhere.

The matrix B_N has dimension $8N \times 6(N+1)^2$. On juxtaposing systems (34) and (35) we obtain an overdetermined nonlinear system of $6(N+1)^2 + 8N$ equations in $6(N+1)^2$ unknowns. Schematically this system can be written as

$$\mathbf{F}(\mathbf{X}) = \mathbf{0}, \tag{36}$$

that is solved via Newton–Raphson algorithm

$$\left[\mathbf{J}(\mathbf{X}^n)\right] \Delta \mathbf{X}^n = -\mathbf{F}(\mathbf{X}^n), \qquad \mathbf{X}^{n+1} = \mathbf{X}^n + \Delta \mathbf{X}^n, \tag{37}$$

where $\mathbf{J}(\mathbf{X}^n)$ is the Jacobian of $\mathbf{F}(\mathbf{X})$ evaluated at iteration n. The matrix $\mathbf{J}(\mathbf{X}^n)$ is not square and $\Delta \mathbf{X}^n$ is a least-square solution of $(37)_1$. For convenience, the elements of the Jacobian matrix are reported in the appendix. As initial guess for the Newton's method we take the rectilinear one dimensional axial flow (null transversal velocity) in the (ξ, η) domain

$$\hat{u}(\xi, \eta) = \frac{1 - \eta^2}{4}, \qquad \hat{v}(\xi, \eta) \equiv 0, \qquad \hat{p}(\xi, \eta) = p_{in} \frac{(1 - \xi)}{2}. \tag{38}$$

We remark that $(37)_1$ can also be solved in the following way. We multiply Eq. $(37)_1$ by $[\mathbf{J}(\mathbf{X}^n)]^T$ in order to obtain a square system whose solution can be sought by any iterative or direct method.

5. Lubrication approximation

When the aspect ratio δ is sufficiently "small" we may look for a solution of (16) that can be expressed as a power series of δ. Following [13] it is easy to check that at the leading order the momentum equation reduces to

$$(S_{12})_y = p_x = \left[\mu(\dot{\gamma}) u_y\right]_y, \qquad p_y = 0. \tag{39}$$

Hence

$$p = p(x), \qquad \dot{\gamma} = \frac{1}{2} \left| u_y \right|. \tag{40}$$

In what follows we shall limit our study to the upper part of the channel where $u_y \leqslant 0$ (provided $p_{in} > 0$). We consider the constitutive laws (12), (13) and we determine the zero order solution in the original (x, y) coordinate system. We observe that, because of symmetry

$$S_{12} = y p_x. \tag{41}$$

5.1. Case 1: regularized Bingham fluid

The Bingham apparent viscosity (12) is given by

$$\mu(\dot{\gamma}) = \left(1 + \frac{B}{-\dfrac{u_y}{2} + \varepsilon}\right). \tag{42}$$

Rearranging (39) with $\mu(\dot{\gamma})$ taken from (42) we get

$$\left(u_y\right)^2 - \left(2\varepsilon + 2B + y p_x\right) u_y + 2\varepsilon y p_x = 0, \tag{43}$$

whose only physically acceptable solution is

$$u_y = f\left(p_x, y\right), \tag{44}$$

$$f := \frac{1}{2} \left[\left(2\varepsilon + 2B + y p_x\right) - \sqrt{\left(2\varepsilon + 2B + y p_x\right)^2 - 8\varepsilon y p_x}\right]. \tag{45}$$

Integration of (44) with the no-slip condition provides the longitudinal velocity

$$u(x, y) = -\int_y^{h(x)} f\left(p_x, \tilde{y}\right) d\tilde{y}, \qquad y \in [0, h(x)]. \tag{46}$$

Notice that in (46) the pressure is unknown at this stage. Exploiting mass balance we find

$$v_y = -u_x = f\left(p_x, h\right) h_x + p_{xx} \int_y^{h(x)} \partial f(p_x, \tilde{y}) \, d\tilde{y}, \tag{47}$$

where ∂f denotes the derivative of f with respect to p_x. Integrating (47) between 0 and $h(x)$ (given the no-slip condition at $y = h(x)$ and the symmetry condition on $y = 0$ for the transversal velocity v) we find:

$$0 = f\left(p_x, h\right) h h_x + p_{xx} \left[\int_0^{h(x)} \left(\int_y^{h(x)} \partial f(p_x, \tilde{y}) \, d\tilde{y} \right) dy \right],$$ (48)

which is a second order nonlinear integro-differential equation for the pressure. In conclusion we have to solve the following nonlinear integro-differential BVP

$$\begin{cases} p_{xx} = -\dfrac{f\left(p_x, h\right) h h_x}{\left[\int_0^{h(x)} \left(\int_y^{h(x)} \partial f(p_x, \tilde{y}) \, d\tilde{y} \right) dy \right]}, \\[2em] p|_{x=-1} = p_{in}, \\[1em] p|_{x=1} = 0. \end{cases}$$ (49)

Once the pressure is found, the velocity components in the whole domain are given by

$$u(x, y) = -\int_{|y|}^{h(x)} f\left(p_x, \tilde{y}\right) d\tilde{y},$$ (50)

$$v(x, y) = \text{sign}(y) \left[f(p_x, h) h_x(|y| - h) - p_{xx} \int_{|y|}^h \left(\int_{\tilde{y}}^{h(x)} \partial f(p_x, \tilde{z}) \, d\tilde{z} \right) d\tilde{y} \right].$$ (51)

5.2. Case 2: regularized Casson fluid

When the constitutive law is that of a Casson fluid (8), proceeding as in the Bingham case we find:

$$u_y = g(p_x, y),$$ (52)

$$g := \frac{1}{2} \left[\left(\sqrt{\epsilon} + \sqrt{B} - \sqrt{-\frac{y p_x}{2}} \right) + \right.$$

$$\left. - \sqrt{\left(\sqrt{\epsilon} + \sqrt{B} - \sqrt{-\frac{y p_x}{2}} \right)^2 + 4 \sqrt{-\frac{y p_x}{2}} \sqrt{\epsilon}} \right]^2.$$ (53)

The equation for the pressure now becomes:

$$\begin{cases} p_{xx} = -\dfrac{g\left(p_x, h_x\right) h h_x}{\left[\int_0^{h(x)} \left(\int_y^{h(x)} \partial g(p_x, \tilde{y}) \, d\tilde{y} \right) dy \right]}, \\[2em] p|_{x=-1} = p_{in}, \\[1em] p|_{x=1} = 0. \end{cases}$$ (54)

The velocity field is again given by (50), (51) provided f is replaced by g, Both integro-differential systems , are solved via spectral collocation exploiting Newton's iterative method.

Recalling (41) we may define the approximating yield surfaces $y = \pm \sigma$ imposing that $|S_{12}| = B$, i.e.

$$\pm \sigma(x) = \mp \frac{B}{p_x(x)}, \qquad \sigma(x) > 0.$$ (55)

5.3. Symmetry properties of the analytical solution

In this subsection we prove some properties of the analytical solution, i.e. for the zero order solution of the lubrication approximation. Although these properties are proved for the analytical solution, we shall see that they are maintained also for the general case of a channel with an aspect ratio not necessarily small (see the results in the numerical section). Moreover, the properties proved here are independent of the particular viscosity function, i.e. they hold true for any choice of $\mu(\dot{\gamma})$. Indeed, all the propositions below are proved using the function f (which is related to the Bingham fluid viscosity), but they remain valid for any other regular viscosity function. We begin by proving the following:

Proposition 1. *At any cross section $\bar{x}$ such that $h_x(\bar{x}) = 0$, the transversal velocity v is such that $v(\bar{x}, y) \equiv 0$ for all $y \in [-h(\bar{x}), h(\bar{x})]$.*

Proof. From (48) we notice that, at any point $\bar{x}$ such that $h_x = 0$, we have that necessarily $p_{xx} = 0$. Hence, from (47) $v_y \equiv 0$ for any y at such a point. Recalling that $v = 0$ at $y = h$ we find that $v \equiv 0$ at any cross section $\bar{x}$ such that $h_x = 0$. In other words we can say that, at any cross section in which the channel profile changes its monotonicity (or simply becomes flat) the transversal velocity must be null. This is confirmed by numerical simulations. $\square$

Proposition 2. *If the channel profile $h(x)$ is an even function, then the pressure gradient $p_x(x)$ is also an even function. As a consequence, $u(x, y)$ is even in x and even in y, $v(x, y)$ is odd in x and odd in y, $S_{12}(x, y)$ is even in x and odd in y and $\sigma(x)$ is even in x.*

Proof. Eq. (48) can be rewritten as

$$-hh_x = \int_0^h dy \int_y^h \frac{\left[f(p_x, \tilde{y})\right]_x}{f(p_x, h)} d\tilde{y}. \tag{56}$$

Since the left hand side of the above is odd in x (h is even and hence h_x is odd), assuming that the quotient under the integral sign is irreducible (we can always eliminate the common factor), we have only two situations:

(C1) $\left[f(p_x, \tilde{y})\right]_x$ (odd in x), $f(p_x, h)$ (even in x), $\tag{57}$

(C2) $\left[f(p_x, \tilde{y})\right]_x$ (even in x), $f(p_x, h)$ (odd in x). $\tag{58}$

In the case (C1), since $f(p_x, h)$ is even, we necessarily have that p_x is even in x and the proof in concluded. In the case (C2) $f(p_x, h)$ is odd, so that

$$f\left(p_x(-x), h(x)\right) = -f\left(p_x(x), h(x)\right), \tag{59}$$

because $h(-x) = h(x)$. Relation (59) implies that

$$f\left(p_x(-x), y\right) = -f\left(p_x(x), y\right), \tag{60}$$

i.e. $f(p_x, y)$ is odd (indeed its derivative in x must be even). As a consequence $f(p_x(0), y) = 0$ for all $y \in [-h(0), h(0)]$. Hence from (44) and from the no-slip condition on u we get

$$u_y(0, y) = f(p_x(0), y) \equiv 0, \quad \Longrightarrow \quad u(0, y) = 0, \qquad \forall \ y \in [-h(0), h(0)]. \tag{61}$$

It is straightforward to show that the above leads to a contradiction. Indeed, defining the discharge

$$Q(x) = \int_{-h(x)}^{h(x)} u(x, y) dy, \tag{62}$$

and recalling mass balance and the no-slip condition, we find

$$Q_x = \int_{-h(x)}^{h(x)} u_x(x, y) dy = -\int_{-h(x)}^{h(x)} v_y(x, y) dy = 0. \tag{63}$$

Therefore

$$0 = Q(0) = \int_{-h(0)}^{h(0)} \underbrace{u(0, y)}_{=0} \, dy = Q(x), \tag{64}$$

i.e. the discharge is identically null on each cross section or, in other words, $u(x, y) \equiv 0$ in the whole domain. From (44), (45) we find that, if $u \equiv 0$ then $p_x \equiv 0$, i.e. $p = const$, which is compatible with the boundary conditions $p(-1) = p_{in}$, $p(1) = 0$ only if $p_{in} = 0$. Therefore, for any $p_{in} > 0$ only (C1) can be true. The symmetries for u, v, S_{12} and σ follow from the definitions (50), (51), (41), (55). This concludes the proof of Proposition 2. $\square$

Proposition 3. *Let us consider the problems with channel walls $h(x)$ and $\bar{h}(x)$, with $\bar{h}(x) = h(-x)$ (even reflection). Let us denote by (u, v, p), $(\bar{u}, \bar{v}, \bar{p})$ the relative solutions and let us assume that the boundary conditions for the pressure are the same for both problems, i.e.*

$$p(-1) = p_{in}, \quad p(1) = 0, \qquad \bar{p}(-1) = p_{in}, \quad \bar{p}(1) = 0. \tag{65}$$

Then

$$
\begin{cases}
\bar{u}(x, y) = u(-x, y), \\[2mm]
\bar{v}(x, y) = -v(-x, y), \\[2mm]
\bar{p}(x) = p_{in} - p(-x), \\[2mm]
\bar{S}_{12}(x, y) = S_{12}(-x, y), \\[2mm]
\bar{\sigma}(x) = \sigma(-x).
\end{cases}
\tag{66}
$$

Proof. Suppose $p(x)$ is a solution of . Then, also $p(x) + k$ (with $k \in \mathbb{R}$) is a solution with boundary conditions $p_{in} + k$ at $x = -1$ and k at $x = 1$. Hence the pressure gradient p_x depends only on the pressure drop $\Delta p = p_{in} - 0 = p_{in}$. The function $\tilde{p}(x) = p(x) - p_{in}$ thus satisfies the problem

$$
\begin{cases}
\tilde{p}_{xx} = -\dfrac{f\left(\tilde{p}_x, h\right) h h_x}{\left[\int_0^{h(x)} \left(\int_y^{h(x)} \partial f(\tilde{p}_x, \tilde{y})\, d\tilde{y}\right) dy\right]}, \\[6mm]
\tilde{p}|_{x=-1} = 0, \\[4mm]
\tilde{p}|_{x=1} = -p_{in}.
\end{cases}
\tag{67}
$$

With respect to the pressure $\tilde{p}(x)$, the velocity components remain unchanged, namely $\tilde{u}(x, y) = u(x, y)$, $\tilde{v}(x, y) = v(x, y)$, since $\tilde{p}_x = p_x$. Now consider the new channel profile and the new pressure

$$
\begin{cases}
\bar{h}(x) = h(-x), \qquad \text{(even reflection)}, \\[2mm]
\bar{p}(x) = -\tilde{p}(-x) = p_{in} - p(-x).
\end{cases}
\tag{68}
$$

It is straightforward to verify that

$$
\bar{p}_x(x) = \tilde{p}_x(-x) = p_x(-x),
\tag{69}
$$

$$
\bar{p}_{xx}(x) = -\tilde{p}_{xx}(-x) = -p_{xx}(-x),
\tag{70}
$$

and that $\bar{p}(x)$ satisfies

$$
\begin{cases}
\bar{p}_{xx} = -\dfrac{f\left(\bar{p}_x, \bar{h}\right) \bar{h} \bar{h}_x}{\left[\int_0^{\bar{h}(x)} \left(\int_y^{\bar{h}(x)} \left(f(\bar{p}_x, \tilde{y})\right)_{\bar{p}_x} d\tilde{y}\right) dy\right]}, \\[6mm]
\bar{p}|_{x=-1} = p_{in}, \\[4mm]
\bar{p}|_{x=1} = 0.
\end{cases}
\tag{71}
$$

Therefore $\bar{p}(x)$ represents the pressure field for the channel with profile $\bar{h}(x)$ at the zero order approximation. Now consider the solution $\bar{u}(x, y)$ relative to $\bar{p}_x$. We find

$$
\bar{u}(x, y) = -\int_{|y|}^{\bar{h}(x)} f\left(\bar{p}_x(x), \tilde{y}\right) d\tilde{y} = -\int_{|y|}^{h(-x)} f\left(p_x(-x), \tilde{y}\right) d\tilde{y} = u(-x, y),
\tag{72}
$$

which proves that $\bar{u}(x, y) = u(-x, y)$, the first of (66). Proceeding in the same way for $\bar{v}(x, y)$ (see (51)) one can easily find that $\bar{v}(x, y) = -v(-x, y)$, i.e. the second of (66). Recalling the definition of $\tilde{p}(x)$ and $\bar{p}(x)$ we also verify that $\bar{p}(x) = p_{in} - \tilde{p}(-x) = p_{in} - p(-x)$, i.e. the third of (66). The fourth and fifth of (66) comes directly from (41), (55) and the proof is concluded. $\square$

6. Numerical simulations and discussion

In this section, we present the numerical results obtained solving the discretized problem (30), (31) by the spectral collocation method introduced earlier. We also compare the numerical solution with the analytical solution that can be found when the aspect ratio δ is "small" (asymptotic solution). The aim of these numerical simulations is to visualize the position of the yield surfaces
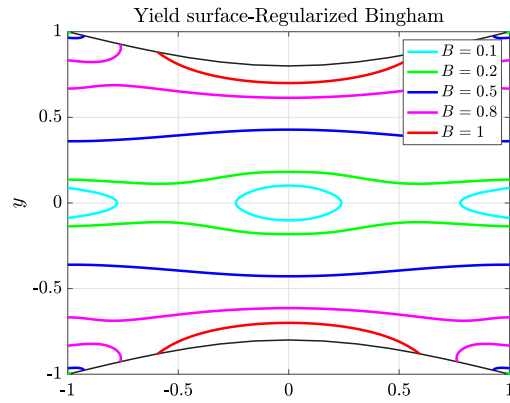
Fig. 3. Yield stress contour plot: profile 1; $p_{in} = 2.5$, $\delta = 1$ (Bingham).
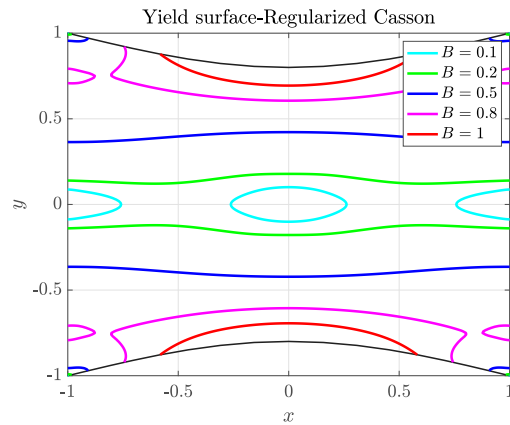

Fig. 4. Yield stress contour plot: profile 1; $p_{in} = 2.5$, $\delta = 1$ (Bingham).

within the flow. The identification of these interfaces is of crucial importance, because it allows one to discriminate between the "rigid" and fluid zone. We recall that the yield surface of a regularized viscoplastic fluid is not a "true" yield surface, because in the regularized model a "real" unyielded region does not exist. The comparison with the available analytical solution is also very important, since it allows us to validate our numerical scheme.

In all the simulations the dimension of the collocation grid is $(N + 1) \times (N + 1)$ with $N = 20$. An increase of N does not affect significantly the accuracy of the solution. In what follows the regularization parameter is $\varepsilon = 0.01$. We consider three different channel profiles, namely:

$$Profile\ 1\ (non-monotone): \quad h = 1 - \frac{1}{5} \sin\left[\frac{\pi}{2}(x+1)\right]; \tag{73}$$

$$Profile\ 2\ (divergent): \quad h = \frac{4}{5} - \frac{1}{5} \cos\left[\frac{\pi}{2}(x+1)\right]; \tag{74}$$

$$Profile\ 3\ (convergent): \quad h = \frac{4}{5} + \frac{1}{5} \cos\left[\frac{\pi}{2}(x+1)\right]. \tag{75}$$

The choice of the three profiles is made to visualize the yield surface behavior in case of a divergent, convergent and non monotone wall functions. We do not have a specific application in mind, so we try to remain as general as possible considering three different types of monotonicity of the channel walls. Since we are dealing with viscoplastic fluids, we have considered two of the mostly used viscoplastic models: the Bingham and the Casson model. We begin by considering an aspect ratio $\delta = 1$. In Figs. 3, 5, 7 we plot the yield surfaces $|\mathbb{S}| = B$ for the Bingham flow for $B = 0.1, 0.2, 0.5, 0.8, 1$. In Figs. 4, 6, 8 we plot the yield surfaces $|\mathbb{S}| = B$ for the Casson flow with the same values of B. In both cases $p_{in} = 2.5$. Figs. 3, 4 are relative to profile 1, Figs. 5, 6 are relative to profile 2, Figs. 7, 8 are relative to profile 3. We notice that, for fixed B and p_{in} the unyielded region of the Casson fluid is "slightly" larger than that of the Bingham fluid.

As observed in Remark 1, there is always an unyielded region in proximity of the points $(\pm 1, 0)$. This is evident in all Figs. 3–8. For "small" values of B these regions are not connected (separated isles), but as B is increased they join together becoming a unique unyielded central core. As B is increased further, the unyielded region expands, eventually occupying the whole domain (for sufficiently large values of B). In case $h(x)$ is given by profile 1 (symmetric with respect to the y axis), we notice also the presence
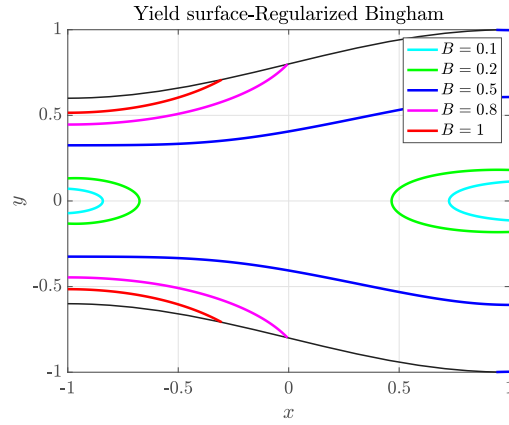
Fig. 5. Yield stress contour plot: profile 2; $p_{in} = 2.5$, $\delta = 1$ (Bingham).
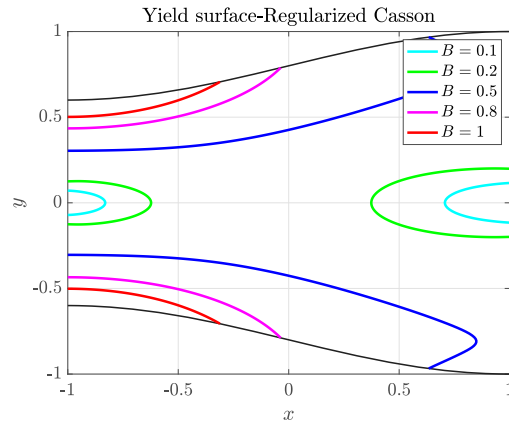

Fig. 6. Yield stress contour plot: profile 2; $p_{in} = 2.5$, $\delta = 1$ (Casson).

of a separated unyielded isle centered in $(0, 0)$ for small B, see Figs. 3, 4. The presence of this central unyielded isle, which is not present in the case of profiles 2 and 3 no matter how small B is, is due to the fact that $h_x(0) = 0$. Indeed, from Proposition 1, we know that $v(0, y) \equiv 0$ if $h_x(0) = 0$ (actually we have proved this property for "small" δ, but let us suppose here that Proposition 1 holds true for any δ). This means that $v_y(0, y) \equiv -u_x(0, y) \equiv 0$. Recalling that, because of symmetry, $u_y(x, 0) \equiv v_x(x, 0) \equiv 0$ it is easy to verify that $\dot{\gamma}(0, 0) = 0$. Hence, there must be a neighborhood of $(0, 0)$ in which the fluid is unyielded (as evident from Figs. 3, 4). When considering profiles 2 and 3 the wall function is such that $h_x(x) \neq 0$ for all $x \in (-1, 1)$ and no internal unyielded region is present, irrespectively of the smallness of B.

Indicating the dependence of the tensor $\mathbb{S}$ on the Bingham number B, i.e. $\mathbb{S}(x, y; B)$ (the solution of the flow problem clearly depends on B) and defining the unyielded domain

$$\Omega_B = \left\{ (x, y) \in \Omega : \ |\mathbb{S}(x, y; B)| \leqslant B \right\} \subseteq \Omega, \tag{76}$$

with

$$\Omega = \left\{ (x, y) : \ x \in [-1, 1], \ y \in [-h(x), h(x)] \right\}, \tag{77}$$

being the flow domain, we have that the function

$$\mathcal{F}(B) = \text{ measure } (\Omega_B) : [0, \infty) \to [0, \text{measure}(\Omega)], \tag{78}$$

is a non decreasing function of B bounded from above by measure(Ω). Physically this means that the "unyielded" part of the fluid enlarges as the yield limit τ_y^* increases.

In Figs. 9–14 we plot the yield surfaces $|\mathbb{S}| = B$ keeping B fixed and letting p_{in} vary. We take $\delta = 1$ and $B = 0.5$. Figs. 9, 10 are relative to profile 1, Figs. 11, 12 are relative to profile 2, Figs. 13, 14 are relative to profile 3. The inlet pressure values are $p_{in} = 1.2, 3, 5, 8$. Looking at Figs. 9–14 we observe that the increase of the pressure results in an expansion of the yielded region, as physically expected (the overall stress becomes larger as the pressure drop p_{in} is increased). The behavior of the unyielded isles
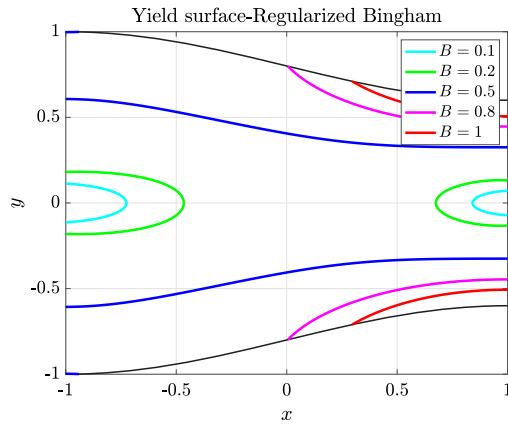
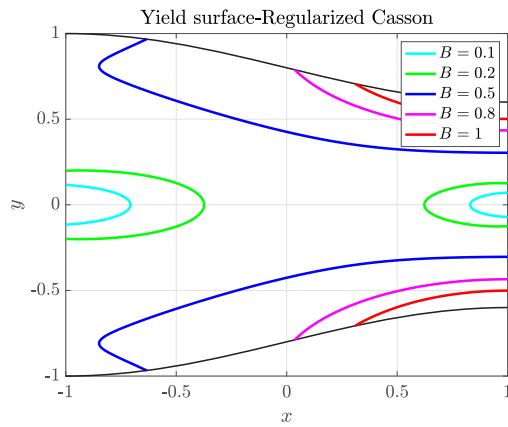**Fig. 7.** Yield stress contour plot: profile 3; $p_{in} = 2.5$, $\delta = 1$ (Bingham).

Fig. 8. Yield stress contour plot: profile 3; $p_{in} = 2.5$, $\delta = 1$ (Casson).
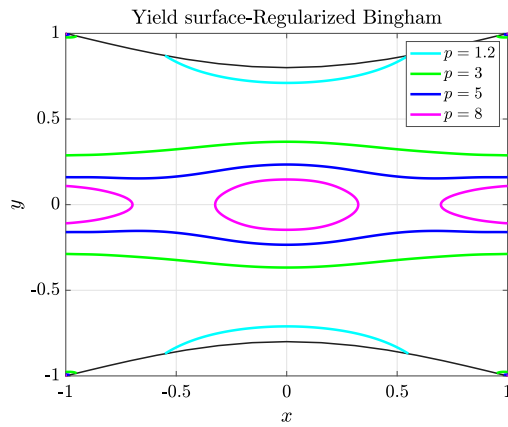

Fig. 9. Yield stress contour plot: profile 1; $B = 0.5$, $\delta = 1$ (Bingham).

centered in $(\pm 1, 0)$ (and also in $(0, 0)$ in the case of profile 1) is the same of that depicted in Figs. 3–8 (i.e. for varying B). These separated isles are formed for "sufficiently" large p_{in}, while for smaller values of p_{in} they are connected in a unique central core. Although the unyielded isles are always present for any value of p_{in} (no matter how large), there exists a threshold value for p_{in} (approximately equal to 1) below which the entire fluid domain becomes unyielded. As in the previous cases, here the unyielded region, for fixed B and p_{in} is larger in the Casson fluid. Analogously to the case of varying B, we may now indicate the dependence
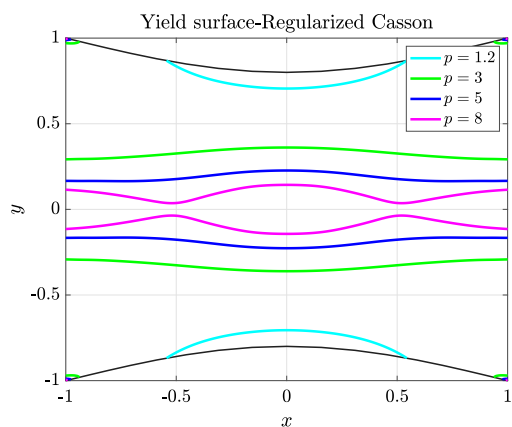
13

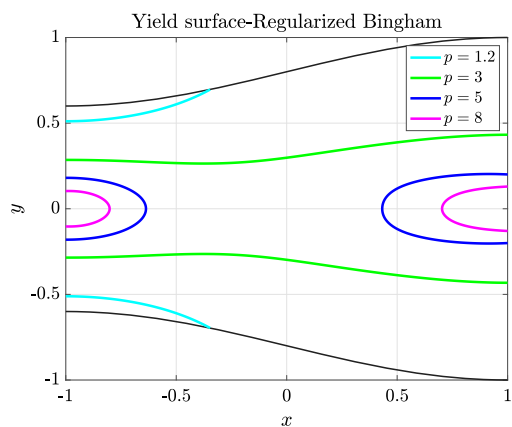**Fig. 10.** Yield stress contour plot: profile 1; $B = 0.5$, $\delta = 1$ (Casson).

Fig. 11. Yield stress contour plot: profile 2; $B = 0.5$, $\delta = 1$ (Bingham).
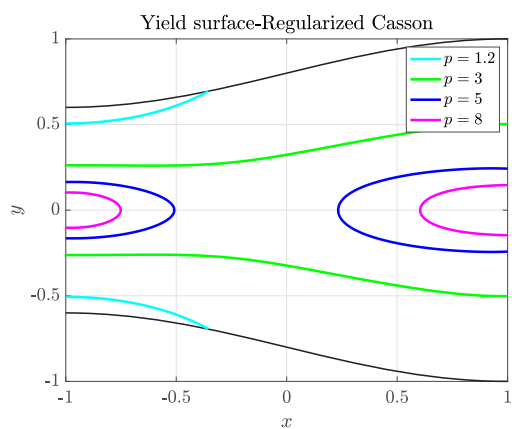

Fig. 12. Yield stress contour plot: profile 2; $B = 0.5$, $\delta = 1$ (Casson).
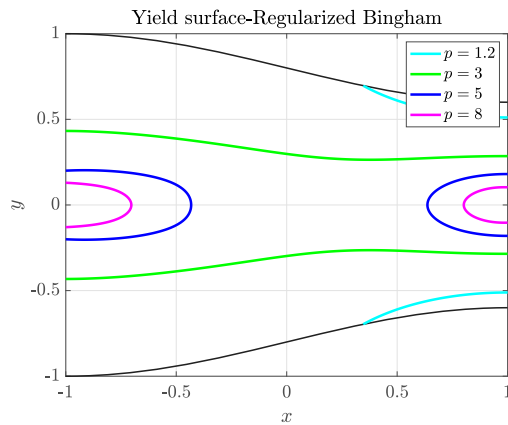
Fig. 13. Yield stress contour plot: profile 3; $B = 0.5$, $\delta = 1$ (Bingham).
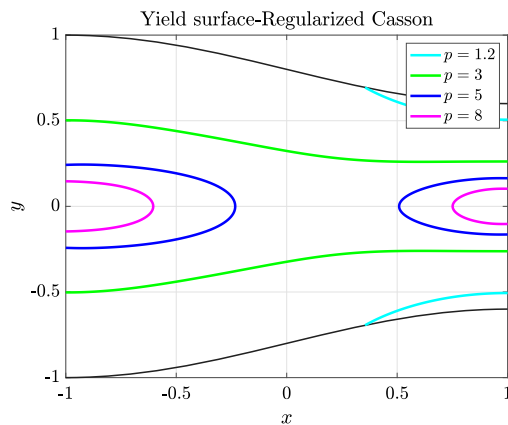

Fig. 14. Yield stress contour plot: profile 3; $B = 0.5$, $\delta = 1$ (Casson).

of the stress $\mathbb{S}$ on p_{in} and write

$$\Omega_{p_{in}} = \left\{ (x,y) \in \Omega : \ |\mathbb{S}(x,y;p_{in})| \leqslant B \right\} \subseteq \Omega, \tag{79}$$

where now B is fixed. The function

$$\mathcal{G}(p_{in}) = \ \text{measure} \ (\Omega_{p_{in}}) : [0,\infty) \to [0, \text{measure}(\Omega)] \tag{80}$$

is now a non increasing function bounded from above by the value $\hat{F} = \text{measure}(\Omega)$. From the physical point of view, we have proven that when the applied force (pressure drop) is increased the yielded part of the fluid enlarges because the overall stress in the fluid becomes larger. In this case the isles centered at the inlet and outlet of the channel becomes smaller. The critical pressure drop at which the domain becomes essentially yielded depends, of course, on the specific value of the yield stress. In other words, the larger is the yield stress the larger is the pressure drop needed to yield the fluid in the whole domain.

To conclude our discussion we now compare the numerical solution with the lubrication solution which was determined in Section 5. This comparison can be used as a validation of our numerical scheme. We begin by comparing the approximating yield surfaces. We plot the numerical (continuous) and analytical (stars) yield surfaces for the Bingham and Casson flows for various values of B, see Figs. 15–16. The pressure drop is $p_{in} = 5$. We immediately notice that for small δ (lubrication flow) the monotonicity of the yield surface is the same of that of the channel profile, Figs. 15–16. This is not true if $\delta \in O(1)$, as evident from Figs. 13, 14. From (55) we see that the zero order solution does not allow the formation of non-connected unyielded regions (isles) and $\sigma(x) > 0$.

In Figs. 17–18 we plot the numerical (continuous) and analytical (stars) longitudinal velocity at cross sections $x = -0.5878, 0.1564$, 0.8090. Here $B = 1$, $p_{in} = 15$ and $\delta = 0.01$. For the sake of simplicity, we have considered only one profile and we have not reported the comparison plots of the transversal velocity and of the pressure, but the results are analogous to those of the axial velocity, see Figs. 17–18. We observe that, at any cross section, the axial velocity resembles the classical "flat" profile of viscoplastic flows. This is more evident in the Bingham flow than in the Casson flow. The "flatness" of the velocity depends on the pressure drop. The larger the pressure drop p_{in}, the "flatter" the velocity profile in the unyielded region.
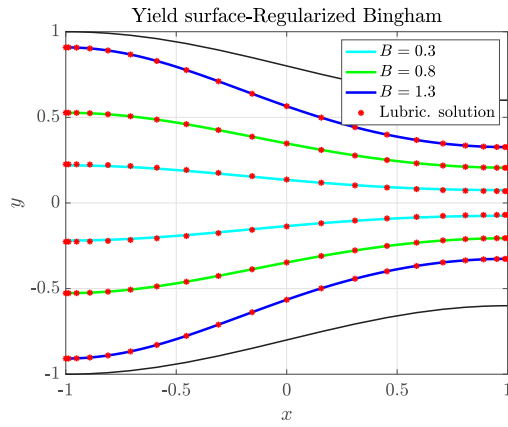
Fig. 15. Yield surfaces comparison: numerical (continuous), analytical (starred), profile 3, $p_{in} = 5$, $\delta = 0.01$ (Bingham).
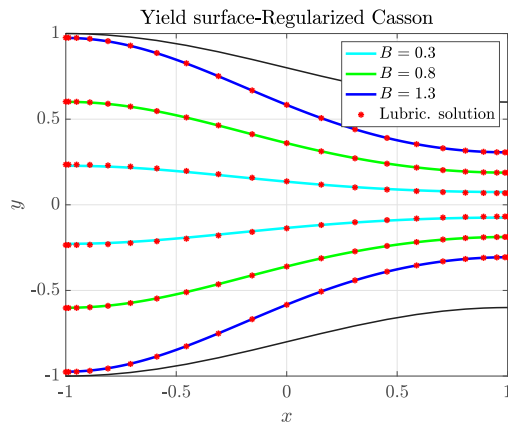

Fig. 16. Yield surfaces comparison: numerical (continuous), analytical (starred), profile 3, $p_{in} = 5$, $\delta = 0.01$ (Casson).

Fig. 17. Axial velocity u comparison at different cross sections: numerical (continuous), analytical (starred), profile 3, $p_{in} = 15$, $B = 1$, $\delta = 0.01$, (Bingham).

To quantify the discrepancy between the numerical and lubrication solution, we have also evaluated the relative error (% percentage) between the numerical and analytical velocity (sup norm), see Table 1 (Bingham), Table 2 (Casson) for the three profiles with δ ranging from 0.01 to 0.8.

We notice that for small values of δ ($\delta < 0.1$) the relative error is not larger than 1%. This proves the accuracy of the numerical solution and the robustness of the numerical scheme.
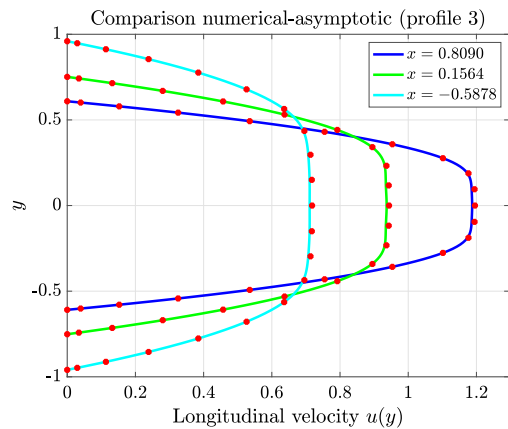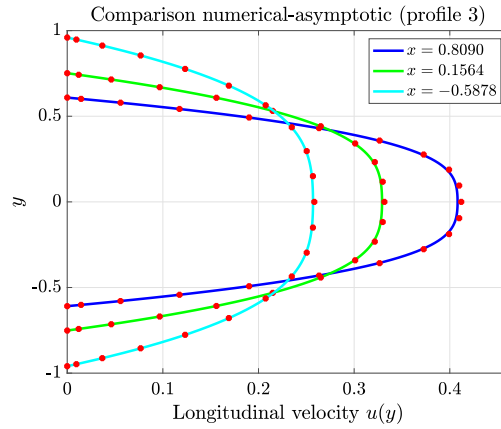
Fig. 18. Axial velocity u comparison at different cross sections: numerical (continuous), analytical (starred), profile 3, $p_{in} = 15$, $B = 1$, $\delta = 0.01$, (Casson).

Table 1
Relative error between the numerical and analytical axial velocity. $N = 20$, Bingham fluid, $B = 0.8$ and $p_{in} = 5$.

δ	profile 1	profile 2	profile 3
0.01	0.67	0.78	0.78
0.1	1.11	0.95	0.95
0.2	2.29	2.48	2.48
0.3	4.49	5.21	5.21
0.8	19.02	26.46	26.46

Table 2
Relative error between the numerical and analytical axial velocity. $N = 20$, Casson fluid, $B = 0.8$ and $p_{in} = 5$.

δ	profile 1	profile 2	profile 3
0.01	0.26	0.36	0.36
0.1	0.53	0.41	0.41
0.2	1.44	1.37	1.37
0.3	2.82	3.04	3.04
0.8	13.88	17.81	17.81

As expected, the error increases with δ, for all the channel profiles. Notice that the errors for profiles 2 and 3 are identical because of the symmetry properties discussed in Section 5.3. This result indicates that the symmetry features that were proved for the lubrication solution hold also for a channel with arbitrary aspect ratio and represents a further validation of our numerical scheme.

7. Conclusions and perspectives

We have proposed a numerical scheme based on spectral collocation method for the incompressible creeping flow of a non-Newtonian fluid in a non-uniform symmetric channel. The flow is driven by a given pressure drop p_{in} and we have assumed no-slip condition on the channel walls (minor changes allow one to consider the case in which the flow is driven by an imposed fixed flow rate). In particular we have focused on a regularized Bingham fluid and a regularized Casson fluid. We have not focussed on a specific application and considered general walls functions (convergent, divergent and non-monotone). The non dimensional governing equations (mass and momentum balance) exhibit non-dimensional groups that contain the parameter δ representing the ratio between the characteristic length and width of the channel. When δ is "small" the zero order solution of the lubrication approximation (asymptotic solution expanded around δ) has been found explicitly. We have proved some symmetry properties of this solution (u, v, p) in a rigorous way. After transforming the flow domain in the spectral domain $[-1, 1]^2$ we have discretized the differential problem by means of spectral differentiation operators, obtaining a non-square nonlinear system that contains also the boundary conditions. This system, which is overdetermined, has been solved via Least Square exploiting the Newton–Raphson algorithm.

We have performed the numerical simulations for three types of wall profiles: i) non-monotone; ii) convergent; iii) divergent. To validate the numerical scheme we have compared the numerical solution with the analytical solution for small δ (zero order approximation). The comparison has shown a very good agreement for both Bingham and Casson fluids ($\delta \lesssim 0.1$). We have also observed that the symmetry properties, that were proved in the lubrication case, are still valid for $\delta \in O(1)$. To pinpoint the

"approximating" yield surfaces we have plotted the level set of the stress corresponding to the yield limit B. For a fixed yield stress and pressure drop, the unyielded regions of the Casson fluid are "slightly" larger that those of the Bingham fluid. We have also proved that, for symmetry reasons, the regions in proximity of the points $(\pm 1, 0)$ are always unyielded.

We have shown that when the driving force (pressure drop) increases, the yielded domain enlarges because of the increase of the internal stress of the fluid. We have also shown that, because of symmetry, unyielded isles are present at the inlet/outlet of the channel (and also in the center in case of symmetric walls), independently of the applied pressure drop and yield limit. We have finally proven that the critical pressure drop at which the yielded domain practically occupies the whole flow domain depends on the specific value of the yield stress. More precisely, the larger is the yield stress the larger is the pressure drop needed to yield the flow in the whole domain.

Although we have shown the efficiency of the method for two particular regularized viscoplastic fluids, our numerical scheme can be easily adapted to any generalized Newtonian fluid simply modifying the function that defines the apparent viscosity $\mu(\dot{\gamma})$. Furthermore, the method can be also extended to fluids with pressure and temperature dependent viscosity [10] or fluids with constitutive equations of implicit type [11,31]. These extensions will be the subject of forthcoming papers.

CRediT authorship contribution statement

Lorenzo Fusi: Writing – original draft, Writing – review & editing. **Antonio Giovinetto:** Writing – original draft, Writing – review & editing.

Acknowledgments

Appendix

A.1. Jacobian matrix

Here we report the components of the Jacobian matrix defined in (37). We write

$$\widehat{\beta}_{N,i,j} = \frac{1}{\widehat{\gamma}_{N,i,j}}, \qquad \widehat{\gamma}_N = \left(\widehat{\gamma}_{N,i,j} \right)_{i,j=1,\dots,(N+1)^2}, \tag{81}$$

$$\frac{\partial \widehat{\mu}_N}{\partial \widehat{u}_N} = \left\{ \mathbb{1}_N \otimes_K \left[\delta^2 \frac{d\widehat{\mu}_N}{d\widehat{\gamma}_N} \otimes_H \widehat{\beta}_N \otimes_H \left(P_{1,N} \widehat{u}_N \right) \right] \right\} \otimes_H P_{1,N} +$$

$$\left\{ \mathbb{1}_N \otimes_K \left[\frac{d\widehat{\mu}_N}{d\widehat{\gamma}_N} \otimes_H 4\widehat{\beta}_N \otimes_H \left(P_{2,N} \widehat{u}_N + \delta^2 P_{1,N} \widehat{v}_N \right) \right] \right\} \otimes_H P_{2,N},$$

$$\frac{\partial \widehat{\mu}_N}{\partial \widehat{v}_N} = \left\{ \mathbb{1}_N \otimes_K \left[\frac{d\widehat{\mu}_N}{d\widehat{\gamma}_N} \otimes_H 4\delta^2 \widehat{\beta}_N \otimes_H \left(P_{2,N} \widehat{u}_N + \delta^2 P_{1,N} \widehat{v}_N \right) \right] \right\} \otimes_H P_{1,N}, \tag{82}$$

where $\otimes_H$ is the *Hadamard product* and $\otimes_K$ is the *Kronecker product*,[3] and where

$$\mathbb{1}_N = [1, \dots, 1] \in \mathbb{R}^{1 \times (N+1)^2}, \qquad \text{(unit row vector)},$$

$$\mathbb{I}_N \in \mathbb{R}^{(N+1)^2 \times (N+1)^2}, \qquad \text{(identity matrix)}, \tag{83}$$

$$\mathbb{O}_N \in \mathbb{R}^{(N+1)^2 \times (N+1)^2}, \qquad \text{(null matrix)}.$$

The components (blocks) of the Jacobian are:

$$J_{12} = J_{13} = J_{16} = \mathbb{O}_N, \qquad J_{11} = \mathbb{I}_N,$$

$$J_{14} = -2\delta \left[\frac{\partial \widehat{\mu}_N}{\partial \widehat{u}_N} \otimes_H \left(\mathbb{1}_N \otimes_K \left(P_{1,N} \widehat{u}_N \right) \right) + \left(\mathbb{1}_N \otimes_K \widehat{\mu}_N \right) \otimes_H P_{1,N} \right],$$

$$J_{15} = -2\delta \left[\frac{\partial \widehat{\mu}_N}{\partial \widehat{v}_N} \otimes_H \left(\mathbb{1}_N \otimes_K \left(P_{1,N} \widehat{u}_N \right) \right) \right],$$

$$J_{21} = J_{23} = J_{26} = \mathbb{O}_N, \qquad J_{22} = \mathbb{I}_N,$$

---

[3] If $A = (a_{i,j})$, $B = (b_{i,j}) \in \mathbb{R}^{m \times n}$ and $C = (c_{i,j}) \in \mathbb{R}^{p \times q}$, $A \otimes_H B = \sum_{\substack{i=1,\dots,m \\ j=1,\dots,n}} a_{i,j} b_{i,j} \mathbf{e}_i \otimes \mathbf{e}_j$ and $A \otimes_K C = (a_{i,j} C) \in \mathbb{R}^{mp \times nq}$.

$$J_{24} = -\left[\frac{\partial \widehat{\mu}_N}{\partial \widehat{u}_N} \otimes_H \left(\mathbb{1}_N \otimes_K \left(P_{2,N}\widehat{u}_N + \delta^2 P_{1,N}\widehat{v}_N\right)\right) + \left(\mathbb{1}_N \otimes_K \widehat{\mu}_N\right) \otimes_H P_{2,N}\right],$$

$$J_{25} = -\left[\frac{\partial \widehat{\mu}_N}{\partial \widehat{v}_N} \otimes_H \left(\mathbb{1}_N \otimes_K \left(P_{2,N}\widehat{u}_N + \delta^2 P_{1,N}\widehat{v}_N\right)\right) + \left(\mathbb{1}_N \otimes_K \widehat{\mu}_N\right) \otimes_H \delta^2 P_{1,N}\right],$$

$$J_{31} = J_{32} = J_{36} = \mathbb{O}_N, \qquad J_{33} = \mathbb{I}_N,$$

$$J_{34} = -2\delta\left[\frac{\partial \widehat{\mu}_N}{\partial \widehat{u}_N} \otimes_H \left(\mathbb{1}_N \otimes_K \left(P_{2,N}\widehat{v}_N\right)\right)\right],$$

$$J_{35} = -2\delta\left[\frac{\partial \widehat{\mu}_N}{\partial \widehat{v}_N} \otimes_H \left(\mathbb{1}_N \otimes_K P_{2,N}\widehat{v}_N\right) + \left(\mathbb{1}_N \otimes_K \widehat{\mu}_N\right) \otimes_H P_{2,N}\right],$$

$$J_{43} = J_{44} = J_{45} = \mathbb{O}_N, \qquad J_{41} = \delta P_{1,N}, \qquad J_{42} = P_{2,N}, \qquad J_{46} = -P_{1,N},$$

$$J_{51} = J_{54} = J_{55} = \mathbb{O}_N, \qquad J_{52} = \delta^2 P_{1,N}, \qquad J_{53} = \delta P_{2,N}, \qquad J_{56} = -P_{2,N},$$

$$J_{61} = J_{62} = J_{63} = J_{66} = \mathbb{O}_N, \qquad J_{64} = P_{1,N}, \qquad J_{65} = P_{2,N}.$$

A.2. Nomenclature

Variable	Name	Unit	Variable	Name	Unit
ρ^*	Density	kg/m^3	Re	Reynolds number	
$\mathbf{v}^*$	Velocity	m/s	B	Bingham number	
$\mathbf{x}^*$	Length	m	δ	Aspect ratio	
τ_y^*	Yield stress	Pa	$\mathbb{D}^*$	Strain rate tensor	s^{-1}
μ_o^*	Viscosity	Pa s	$\mathbb{S}^*$	Stress tensor	Pa
p^*	Pressure	Pa	t^*	Time	s
L^*	Length	m			
H^*	Length	m			

References

[1] M. Bercovier, M. Engelman, A finite-element method for incompressible non-Newtonian flows, J. Comput. Phys. 36 (3) (1980) 313–326.

[2] C. Bernardi, C. Canuto, Y. Maday, Spectral approximations of the Stokes equations with boundary conditions on the pressure, SIAM J. Numer. Anal. 28 (2) (1991) 333–362.

[3] E.C. Bingham, Fluidity and Plasticity, vol. 2, McGraw-Hill, 1922.

[4] D. Boffi, F. Brezzi, M. Fortin, et al., Mixed Finite Element Methods and Applications, vol. 44, Springer, 2013.

[5] N. Casson, Flow equation for pigment-oil suspensions of the printing ink-type, in: Rheology of Disperse Systems, Pergamon Press, 1959, pp. 84–104.

[6] F.Z. Duraihem, M. Nazeer, F. Hussain, S. Saleem, Electro-osmotic particulate flow of non-Newtonian fluid in a bulged out cavity with lubrication: Electro-osmotic dewatering approach, Comput. Part. Mech. (2023) 1–10.

[7] A. Fatima, S. Turek, A. Ouazzi, M.A. Afaq, An adaptive discrete Newton method for regularization-free Bingham model, in: Proceedings of the YIC 2021-VI ECCOMAS Young Investigators Conference, Editorial Universitat Politècnica de València, 2022, pp. 180–189.

[8] I. Frigaard, C. Nouar, On the usage of viscosity regularisation methods for visco-plastic fluid flow computation, J. Non-Newtonian Fluid Mech. 127 (1) (2005) 1–26.

[9] I. Frigaard, D. Ryan, Flow of a visco-plastic fluid in a channel of slowly varying width, J. Non-Newtonian Fluid Mech. 123 (1) (2004) 67–83.

[10] L. Fusi, Non-isothermal flow of a Bingham fluid with pressure and temperature dependent viscosity, Meccanica 52 (2017) 3577–3592.

[11] L. Fusi, Channel flow of viscoplastic fluids with pressure-dependent rheological parameters, Phys. Fluids 30 (7) (2018).

[12] L. Fusi, A. Farina, A mathematical model for Bingham-like fluids with visco-elastic core, Zeitschrift für angewandte Mathematik und Physik ZAMP 55 (2004) 826–847.

[13] L. Fusi, A. Farina, K.R. Rajagopal, L. Vergori, Channel flows of shear-thinning fluids that mimic the mechanical response of a Bingham fluid, Int. J. Non-Linear Mech. 138 (2022) 103847.

[14] L. Fusi, A. Farina, F. Rosso, Squeeze flow of a Bingham-type fluid with elastic core, Int. J. Non-Linear Mech. 78 (2016) 59–65.

[15] L. Fusi, A. Farina, F. Rosso, S. Roscani, Pressure driven lubrication flow of a Bingham fluid in a channel: A novel approach, J. Non-Newtonian Fluid Mech. 221 (2015) 66–75.

[16] R. Glowinski, A. Wachs, On the numerical simulation of viscoplastic fluid flow, in: Handbook of Numerical Analysis, vol. 16, Elsevier, 2011, pp. 483–717.

[17] W. Heinrichs, Least-squares spectral collocation for the Navier–Stokes equations, J. Sci. Comput. 21 (2004) 81–90.

[18] W. Heinrichs, Least-squares spectral collocation with the overlapping Schwarz method for the incompressible Navier–Stokes equations, Numer. Algorithms 43 (2006) 61–73.

[19] W.H. Herschel, R. Bulkley, Konsistenzmessungen von Gummi-Benzollösungen, Kolloid-Zeitschrift 39 (1926) 291–300.

[20] J. Hron, J. Málek, K. Rajagopal, Simple flows of fluids with pressure–dependent viscosities, Proc. R. Soc. Lond. Ser. A Math. Phys. Eng. Sci. 457 (2011) (2001) 1603–1622.

[21] R.R. Huilgol, G.C. Georgiou, Fluid Mechanics of Viscoplasticity, Springer, 2015.

[22] R.R. Huilgol, G.C. Georgiou, A fast numerical scheme for the Poiseuille flow in a concentric annulus, J. Non-Newton. Fluid Mech. 285 (2020) 104401.

[23] R.R. Huilgol, Z. You, Application of the augmented Lagrangian method to steady pipe flows of Bingham, Casson and Herschel–Bulkley fluids, J. Non-Newtonian Fluid Mech. 128 (2–3) (2005) 126–143.

[24] M. Nazeer, A.A.A. Ahamdi, A.N. Alzaed, M. Alwetaishi, M.W. Nazir, M.I. Khan, Impact of slip boundary conditions, magnetic force, and porous medium on blood flow of Jeffrey fluid, ZAMM-J. Appl. Math. Mech./Z. Angew. Math. Mech. 102 (10) (2022) e202100218.

[25] M. Nazeer, F. Hussain, M.O. Ahmad, S. Saeed, M.I. Khan, S. Kadry, Y.-M. Chu, Multi-phase flow of Jeffrey Fluid bounded within magnetized horizontal surface, Surf. Interfaces 22 (2021) 100846.

[26] M. Nazeer, F. Hussain, M. Ghafar, M.A. Javed, Investigation of electro-osmotic flow of hafnium particles mixed-up with Casson fluid in convergent geometry: Theoretical study of multiphase flow, in: Partial Differential Equations in Applied Mathematics, vol. 6, Elsevier, 2022, p. 100448.

[27] P. Panaseti, Y. Damianou, G.C. Georgiou, K.D. Housiadas, Pressure-driven flow of a Herschel-Bulkley fluid with pressure-dependent rheological parameters, Phys. Fluids 30 (3) (2018).

[28] T.C. Papanastasiou, Flows of materials with yield, J. Rheol. 31 (5) (1987) 385–404.

[29] V. Pruša, K. Rajagopal, Flow of an electrorheological fluid between eccentric rotating cylinders, Theoret. Comput. Fluid Dynam. 26 (2012) 1–21.

[30] A. Putz, I. Frigaard, D. Martinez, On the lubrication paradox and the use of regularisation methods for lubrication flows, J. Non-Newtonian Fluid Mech. 163 (1–3) (2009) 62–77.

[31] K. Rajagopal, On implicit constitutive theories for fluids, J. Fluid Mech. 550 (2006) 243–249.

[32] P. Saramito, A. Wachs, Progress in numerical simulation of yield stress fluid flows, Rheol. Acta 56 (2017) 211–230.

[33] L.N. Trefethen, Spectral Methods in MATLAB, SIAM, 2000.

[34] C. Truesdell, W. Noll, C. Truesdell, W. Noll, The Non-Linear Field Theories of Mechanics, Springer, 2004.

[35] Z. You, R.R. Huilgol, E. Mitsoulis, Application of the Lambert W function to steady shearing flows of the Papanastasiou model, Int. J. Eng. Sci. 46 (8) (2008) 799–808.